

Reconstructing the gravity gradient anomaly field from surveys with wide line spacing using equivalent source processing: an error analysis

Gary Barnes*

Bridgeporth Ltd., United Kingdom, previously at Arkex Ltd., United Kingdom

Received October 2012, revision accepted June 2013

ABSTRACT

When anomalous gravity gradient signals provide a large signal-to-noise ratio, airborne and marine surveys can be considered with wide line spacing. In these cases, spatial resolution and sampling requirements become the limiting factors for specifying the line spacing, rather than anomaly detectability. This situation is analysed by generating known signals from a geological model and then sub-sampling them using a simulated airborne gravity gradient survey with a line spacing much wider than the characteristic anomaly size. The data are processed using an equivalent source inversion, which is used subsequently to predict and grid the field in-between the survey lines by means of forward calculations. Spatial and spectral error analysis is used to quantify the accuracy and resolution of the processed data and the advantages of acquiring multiple gravity gradient components are demonstrated. With measurements of the full tensor along survey lines spaced at 4×4 km, it is shown that the vertical gravity gradient can be reconstructed accurately over a bandwidth of 2 km with spatial root-mean square errors less than 30%. A real airborne full-tensor gravity gradient survey is presented to confirm the synthetic analysis in a practical situation.

Key words: Gravity, Data processing, Numerical study, Potential field.

INTRODUCTION

When designing airborne or marine gravity gradient surveys, the decision on line spacing is often dictated by a signal-to-noise ratio (SNR) requirement. In order to detect a small anomalous signal in the presence of noise, several survey lines are required to traverse the anomaly so that the noise averages out and the anomaly becomes visible. If N lines cross the anomaly, then the SNR increases by the square root of N . The line spacing for a survey is chosen accordingly to ensure that the target anomalies are detectable with a level of confidence (SNR > 1).

If the geological targets give sufficiently large amplitude, then a single traverse of the anomaly field can be sufficient to provide an adequate SNR. This can happen when shallow

localized anomalies with high-density contrasts such as ore bodies or salt structures are present. Such sources can often provide gravity gradient signals in the tens of Eotvos over distances of several hundred metres to a few kilometres. With current gravity gradiometer technology having noise levels around $10 \text{ E}/\sqrt{\text{Hz}}$ and airborne survey speeds around 65 m/s, an ample SNR can be achieved along a single line for these targets. With ship speeds of 3–5 m/s, this situation is already common-place with marine surveys. The choice of line spacing is then dictated by sampling rather than detectability. Adequate spatial sampling is required to properly image and resolve anomalies. When measuring a single component, to ensure the spatial bandwidth of the target signal is adequately supported, the sample spacing should be less than the vertical distance to the shallowest target (Reid 1980). In the extreme case of deficient sampling, anomalies might be missed altogether as they fall in-between survey lines or their signals can

*E-mail: gary.barnes@bridgeporth.com

be aliased to form apparently wider anomalies. Since gravity gradients have increased power at shorter wavelengths, they are more susceptible to aliasing than conventional gravity measurements. Flying higher automatically builds in an anti-aliasing filter but at the expense of the SNR. Extra care is therefore required at the planning stage to ensure that the survey design makes best use of these high-bandwidth signals.

It is well-known that measurements of field gradients can increase the ability to interpolate data between sampling points (FitzGerald and Holstein 2006). Systems that acquire multiple components of the gravity gradient tensor can therefore produce a processed data set with a resolution that exceeds that implied by the original acquisition pattern. Tensor gridding methods are available in commercial software, achieving typically 50% increases in the resolution (FitzGerald, Paterson and Holstein 2012). Brewster (2011) compared a full-tensor system to a G_{zz} only system and demonstrated that with the extra components, the line spacing can be increased by a factor of 1.55 without compromising the success of resolving anomalies. Using Fourier domain generalized sampling expansions, While, Biegert and Jackson (2008) showed that in theory, the spacing of a series of parallel lines can be increased by 3 times when reconstructing the gravity field using additional measurements of G_{zz} and G_{yz} (where y is the direction across the lines). Tensor components involving the vertical (z) direction are naturally more sensitive to the sources underneath the survey line whereas the horizontally orientated tensors are more sensitive to sources off-line. One would therefore expect a system that combines vertical and horizontal components to be advantageous for accurately reconstructing the gravity field.

The equivalent source method (Dampney 1969) has become a popular technique for processing gravity gradient data. Any number of tensor components can be accommodated through joint inversion into a single density model. The resulting model is used to forward calculate an enhanced field either back at the original measurement points, or to new locations within the boundaries of the survey. The forward calculation can therefore provide both a transformation and a gridding operation that are both guaranteed to produce harmonic fields (Mendonça and Silva 1995). The data are enhanced because the combination of different tensor components during the inversion reduces noise and increases the spatial resolution. Typically, such processing is used to produce a regular grid of field data located at a constant altitude.

Through an eigenvalue analysis, Pilkington (2012) compared the usefulness of different tensor combinations for use in 3D geological density inversions. Assuming gridded input

data centred over the cells of the inversion model, the information content of the measurement sets rather than the sampling was the focus of that study. Rim and Li (2012) took the other extreme, where sampling is severely restricted, by studying what can be inferred from gravity gradient data acquired down a borehole. The goal of the analysis we present here is to demonstrate how processing multiple gravity gradient components using the equivalent source technique can predict the field in-between widely spaced lines of an airborne or marine gravity gradient survey. Sampling and resolution, rather than noise, is therefore the focus of this study and a high SNR is intrinsically assumed. The term 'predict' is used, rather than 'interpolate' because the equivalent source method involves an inversion followed by a forward calculation, which are analogous to the estimation and prediction stages referred to in the broader subject of system modelling. Interpolations do not generally imply an increase in bandwidth of the data but produce smooth surfaces that pass through the measurements. Inverted models, however, can potentially produce signals with a higher bandwidth that might (or might not) predict the true signal variation between widely spaced sample points (Barnes *et al.* 2008).

We define the 'useful resolution' of a gridded data set as the radial bandwidth over which the data accurately and uniformly represent the anomaly field. Over this bandwidth, the radial power spectral density (PSD) of the error in the processed data is less than the PSD of the true anomaly field. The error is made up from all conceivable terms including those relating to imperfect sampling, draped flying conditions, applied and unintentional filtering and any numerical artefacts generated by the processing algorithms. In reality, the instrument noise contributes significantly to the total error budget but this is not the subject of the analysis presented here. For instrument noise analysis, see Barnes *et al.* (2010) and the examples presented by Brewster (2012). A level of confidence is added to limit the useful resolution to the bandwidth where the error PSD is at least some factor smaller than the signal PSD. A factor of two, for example, would give a bandwidth over which one could be highly confident that the data are representing the true signal.

Due to the non-uniform nature of the original sampling, it is very difficult to estimate the useful resolution of the resulting processed and gridded data set theoretically. Assuming cylindrical symmetry, Pederson and Rasmussen (1990) related the radial Nyquist frequency to the geometric mean of the Nyquist frequencies in the x - and y -directions. When a single component is measured, this figure can be used to estimate the useful resolution resulting from a regular set of parallel

survey lines. With gradiometry surveys, there is often a large discrepancy between the Nyquist sampling frequencies along the lines and across the lines where the high bandwidth along the line (100–200 m) can be an order of magnitude different to the sampling across the line (e.g., >1 km). In these cases, the approximated radial Nyquist frequency becomes less accurate as a measure of the resulting useful resolution. The introduction of orthogonal cross-lines and the simultaneous acquisition of multiple components of the field on draped flight patterns further complicate the matter. Simulations are therefore required that take known gravity gradient signals through the sampling and processing procedures followed by numerical error analysis to compare the processed results with the exact answer to estimate the resulting useful resolution.

The Full Tensor Gradiometer (FTG), manufactured by Lockheed Martin consists of three Gravity Gradient Instruments (GGI) mounted on a three-axis stabilized platform (Jekeli 1993). Each GGI contains four accelerometers positioned on a spinning disk and by combining their measurements, the two components of differential curvature in the plane of the disk can be determined. A disk located in the u - v plane would give in-line and cross-components of $(Guu - Gvv)/2$ and Guv respectively. The three GGIs are mounted orthogonally defining Cartesian axes u, v, w , which are tilted 54.7 degrees to the vertical forming what is known as the ‘umbrella’ coordinate system (Brzezowski and Heller 1988). From the six differential curvature components, the complete gravity gradient tensor can be constructed using simple linear algebra.

In the following, the up-lift in resolution by incorporating more components will be analysed by considering the cases of measuring and utilizing a) only G_{zz} , b) G_{zz}, G_{xz}, G_{yz} , c) one vector of differential curvature, d) two vectors and e) all three vectors of differential curvature. The differential curvature components used are those defined by the FTG umbrella coordinate system and the last case essentially represents using the full tensor. The resolution will be assessed by performing error analysis on the predicted and reconstructed G_{zz} anomaly field on a level grid. G_{zz} is chosen as it most closely resembles the anomalous density distribution and contains the highest information content (Pilkington 2012) and therefore best represents the requirements for geological interpretation.

EQUIVALENT SOURCE MODELLING

The equivalent source processing scheme employed is that described by Barnes and Lumley (2011). Equivalent source models are constructed using a regular array of vertical rectangular

prisms defining a top surface that follows the terrain and a bottom surface located at a depth below the lowest point in the terrain. A degree of padding is introduced so that the model spans an area slightly larger than the survey perimeter to accommodate the signal that originates outside of the measurement area. The density within each prism is uniform but varies from prism to prism and the set of prism densities form the variables of the inversion. An optimization algorithm solves for the density distribution, which results in a model whose response fits the measurements in a least squares sense. Subsequent forward calculations from the model can be used to predict the field at locations in-between the original measurements forming the gridding feature of the equivalent source method. Regularization is essential to prevent the inversion from being ill conditioned. Without suitable regularization, even if the inverted model reproduces the measurement data closely, it cannot be used to generate other field components or data at new locations reliably.

The preferred and most popular choice of regularization is to maximize the smoothness of the inverted density distribution by augmenting the optimization with a term proportional to the x, y gradient energy of the density distribution:

$$\text{minimise} \left\{ \sum_{i=1}^N (f(r_i) - m_i)^2 + \alpha \iint \left(\frac{\partial \rho}{\partial x} \right)^2 + \left(\frac{\partial \rho}{\partial y} \right)^2 dx dy \right\}, \quad (1)$$

where $f(r_i)$ is the forward calculation of the field from the model at the position r_i of the i th measurement m_i and ρ represents the density distribution. The constant of proportionality, α , is known as the regularization factor (equivalent to a Lagrange multiplier) and controls the trade-off between the inverted model fitting closely to the data and maximizing the smoothness of its density distribution. Ideally, one would like to increase the regularization factor as much as possible whilst still maintaining a good fit to the measurements. Where there are no measurement data, the regularization acts to interpolate the inverted density distribution and therefore plays an important role when reconstructing the field in these areas.

In the majority of cases, the total signal power is dominated by the terrain contribution, which, on average, has a density contrast of 2.67 g/cm³ relative to the air. In comparison, sub-surface density contrasts rarely exceed 0.5 g/cm³ and by virtue of their depth, produce a lower bandwidth signal. By constructing the equivalent source model to follow the terrain, it automatically accommodates the majority of the terrain signal through the average value of the inverted density. This leaves only the anomaly field to be modelled by

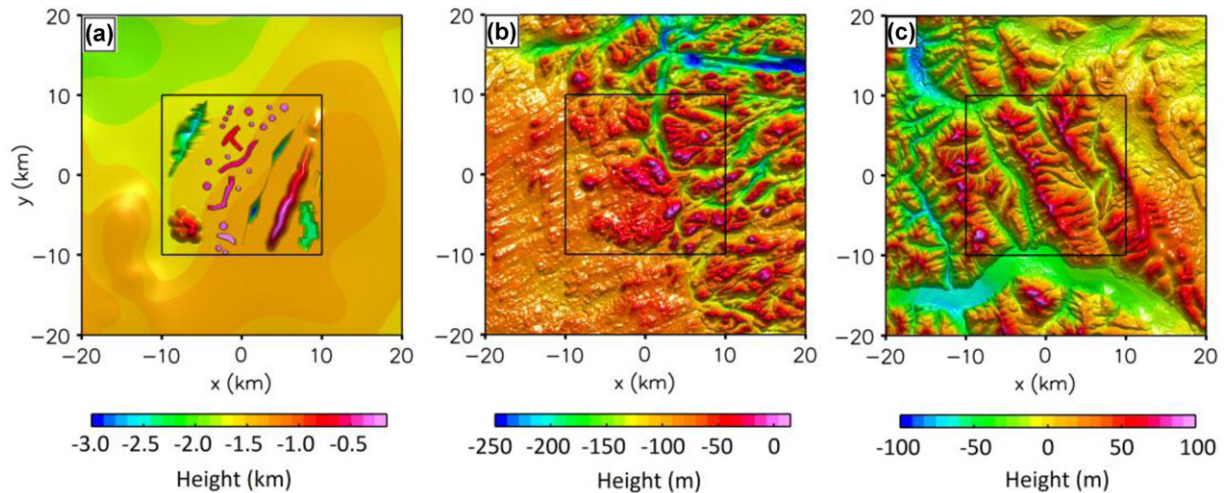


Figure 1 Synthetic geological model. a) Feature layer, b) weathering layer, c) terrain layer. Black square shows the area of interest over which simulated survey data are calculated.

smoothly regularized density distributions, which significantly reduces the risk of the terrain signals from being aliased when inverting data across widely spaced survey lines. Making the terrain term part of the model geometry also allows for an easy way of performing the constant-density terrain correction – by simply removing the average of the inverted density distribution (or subtracting a known terrain density) before performing the forward calculations. Such a data set is often useful as a first-pass anomaly field map for basic qualitative interpretation.

SYNTHETIC TEST MODEL

To perform a proper error analysis, the truth data must be known and therefore synthetic models need to be used. A fictional geological setting was therefore devised, which although might not bear resemblance to reality, was designed to produce signals that have similar characteristics to real survey data. The inspiration for the model was derived from a variety of geological targets that formed the basis of airborne gravity gradient surveys undertaken mainly for hydrocarbon prospecting.

Figure 1(a) shows a gridded horizon representing a set of modelled geological ‘features’ including a failed rift, batholith, salt bodies, transform basins and an anticline. These features are set on a smoothly undulating background surface to provide a long-wavelength signal from the model. Above this surface lies a weathering layer (Fig. 1b), which produces higher bandwidth signals that often interfere with the targets of interest. In close proximity to the weathering layer is the terrain

surface, Fig. 1(c). Both the terrain and weathering layers were adapted from high-resolution LiDAR data acquired during airborne surveys. All layers define solid bodies in the model with associated density values. The terrain body, having the topography as the top and the weathering layer as its base, was given a variable density using random numbers drawn from the normal distribution with a mean of 2.26 g/cm^3 and a standard deviation varying spatially between $0\text{--}0.2 \text{ g/cm}^3$. Zero variation was used for the highest terrain point increasing linearly to 0.2 g/cm^3 for the lowest point. The fluctuation forms the basis for the high-frequency signal generated by density variations within the terrain, especially at the surface where erosion and alteration have occurred. Having greater density variability at the lower elevations is a crude way of simulating the unconsolidated weathering products found at these heights. Further near-surface anomalies were added by carving out areas of the terrain identified as sedimentary fill (such as the valleys shown in Fig. 1c) and filling with lower density material. Other parts of the model were ascribed densities according to the features they represent. The full details of the construction are not important, only the fields generated from the model are of interest in this study. Figure 2(a) shows the forward calculation of G_{zz} to a constant altitude grid at height $z = 100 \text{ m}$ and a pitch of 50 m over the central $(20 \times 20) \text{ km}$ region of the model. This inner region, encompassing the geological features, is designated as the area of interest and the model outside this area serves only to provide the background field. The terrain corrected data (Fig. 2b) are not the model response with the terrain body omitted but the anomaly field calculated by subtracting the forward

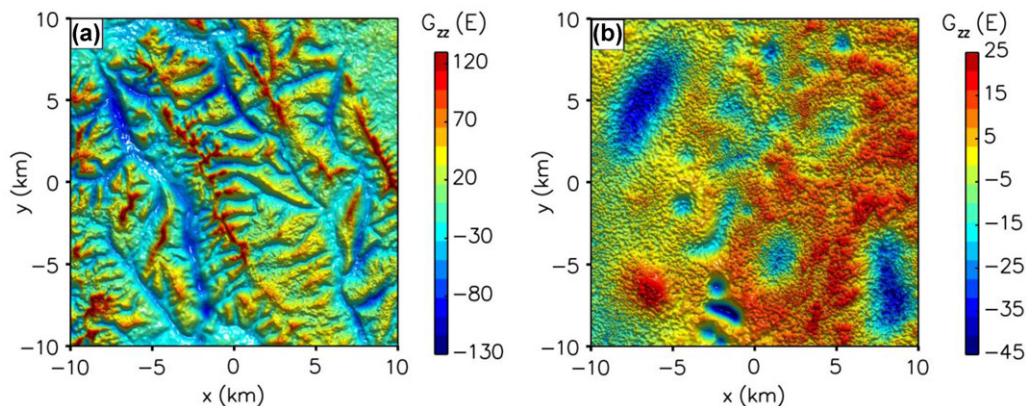


Figure 2 Forward calculations of G_{zz} from the geological model to a 50×50 m grid at 100 m elevation over the area of interest. a) Full signal, b) anomaly field.

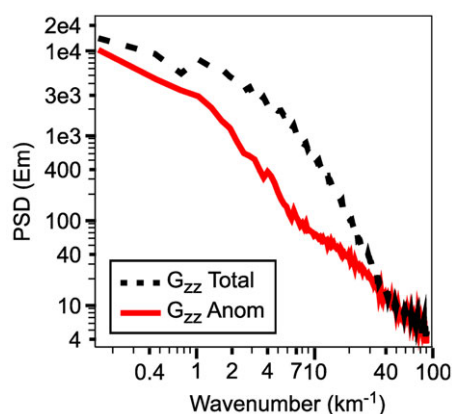


Figure 3 Radial PSDs of model forward calculated G_{zz} and the G_{zz} anomaly field.

calculation of a terrain correction body having the topography as its top, a flat base located at $z = -100$ m and a uniform density of 2.26 g/cm^3 . Note that the actual level of the base of this body is arbitrary since a uniform density Bouguer style slab can be added or removed without affecting the gravity gradient signal. Figure 3 shows the radial PSDs of the total signal and the anomaly field, demonstrating that a constant-density terrain model explains a large percentage of the total signal power.

Figure 2(b) represents the goal of the processing – given values of the full signal sampled along widely spaced flight lines and an accurate digital elevation model of the topography, reconstruct the entire anomaly field as accurately as possible.

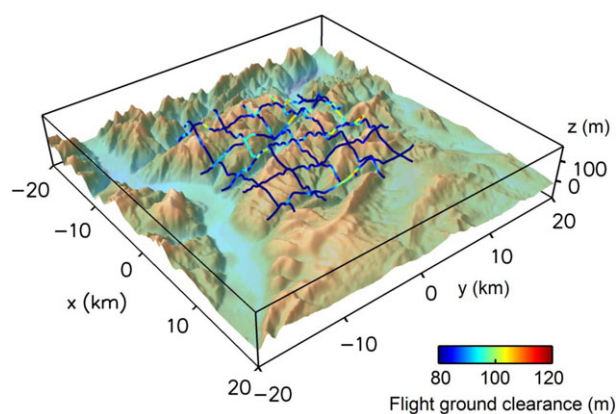


Figure 4 Flight pattern draped over terrain with 4×4 km line spacing. Colour bar shows the ground clearance of the flight pattern.

SIMULATED AIRBORNE ACQUISITION

To ensure that the maximum signal amplitude is measured, airborne gravity gradient surveys are often flown with a draped flight height. A draped surface can be defined as the closest surface to the ground that is also flyable. Once the draped surface is obtained, a minimum safe flying height is added before sampling onto the flight line pattern. Figure 4 shows the resulting draped flight pattern over the model for a survey with north-south and east-west lines separated equally by 4 km. Points along the lines are separated by 1 s intervals and forward calculations of the gravity gradient components from the complete geological model to these locations define the measurements for the equivalent source inversions. The

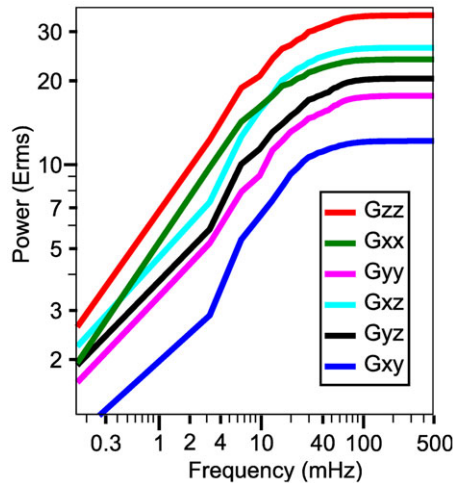


Figure 5 Time-domain cumulative PSDs of simulated airborne gravity gradient components. All signal powers saturate at a bandwidth of approximately 100 mHz.

bandwidths of the synthetic time-domain signals along the lines are all approximately 100 mHz (65 m/s flying speed), see Fig. 5. All gravity gradiometers in commercial use and future instruments under development have bandwidths exceeding this frequency meaning that faithful, undistorted measurements of the signals along the lines can be assumed in these simulations.

RECONSTRUCTING THE ANOMALY FIELD

Equivalent source processing was performed separately for the 5 measurement groups listed in Table 1. In each case, a series of inversions were performed with different regularization factors to build up an L-curve to help determine the most appropriate level of regularization. The preferred solutions were chosen by visually identifying the ‘knee’ points of the L-curves as these positions represent the best compromise be-

tween model regularization and the fit to the input data, see Fig. 6.

The average value was subtracted from the inverted density distributions before forward calculation to incorporate the constant-density terrain correction into the predicted fields (all the inverted density distributions had average values close to the true average of 2.26 g/cm^3 ascribed to the terrain layer in the synthetic model). Forward calculations of G_{zz} were performed to the same grid as that shown in Fig. 2, having a constant altitude of 100 m, which is close to the 103 m median height of the simulated airborne measurement data. Figure 7 compares these forward calculations of the anomaly field with the exact model answer. There are obviously 3 different ways of choosing 1 or 2 GGIs out of the possible 3 GGIs of the FTG. All choices show visually similar results, so therefore only a single case is presented in Fig. 7(d,e). With the large line spacing of 4 km, the shortest wavelength signals originating mostly from the near-surface variable density (appearing as the speckle in the model response of Fig. 7a), are lost in-between the lines but are reproduced more faithfully along the lines where the sampling is much denser. One can see that, as more components are used in the inversion, the accuracy in predicting the field in-between the survey lines improves. The predictions from the G_{zz} inversion (Fig. 7b) deteriorate quickly for field points away from the survey line locations. This can be expected since the G_{zz} component is most sensitive to the sources directly underneath the measurement locations but least sensitive to the anomalies located off-line. The general long-wavelength signal trends are clearly reproduced correctly but a lot of fine details and some anomalies are missing when they fall in-between lines. The group containing G_{zz} , G_{xz} , G_{yz} (Fig. 7c) demonstrates a marked improvement in the reconstructed field away from the lines due to the inclusion of the horizontal gradients. Figure 8 highlights the advantages of measuring more components by showing the RMS error of the reconstructed G_{zz} anomaly field as a function of the distance from the nearest sample point. In this figure, an

Table 1 Useful resolutions of reconstructed G_{zz} data from a $4 \times 4 \text{ km}$ survey. Values represent the radial wavelength down to which the error PSD is less than i) 70% and ii) 50% of the signal PSD.

Measurement Group	Number of independent components	Useful resolution 70% error level	Useful resolution 50% error level
G_{zz}	1	3.3 km	5.7 km
$1 \times \text{GGI}$	2	2.2 km	3.1 km
G_{zz}, G_{xz}, G_{yz}	3	1.6 km	2.6 km
$2 \times \text{GGI}$	4	1.3 km	2.1 km
$3 \times \text{GGI}$	5	1.3 km	2.0 km

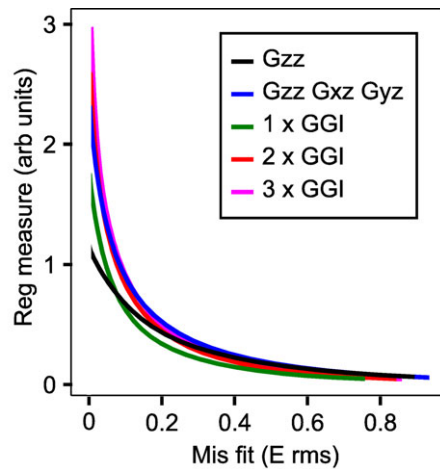


Figure 6 L-curves produced by running equivalent source inversions with different regularization factors for each of the measurements groups listed in Table 1.

error of 0% represents perfect prediction of the full-bandwidth anomaly field, whereas an error of 100% corresponds to a complete absence of a predicted signal, just a smooth interpolation in-between the lines. By comparing the single component (G_{zz}) case to the cases with 2 and 3 GGIs, the error away from the line can be approximately halved by increasing the number of measured components. Note that the errors for the G_{zz} , $\{G_{zz}, G_{xz}, G_{yz}\}$ and full tensor (GGI 1,2,3) cases do not go completely to zero at zero distance but fall to approximately 10%, despite the fact that these groups actually contain G_{zz} measurements directly. This error is due to the regularization that is sacrificing an exact fit to the input data in favour of a more conditioned solution that can better predict the field at new locations. Analysing the solutions either side of the knee points of Fig. 6 confirms that these points of maximum curvature on the L-curve do correspond to the best overall solutions. A more sophisticated regularization scheme,

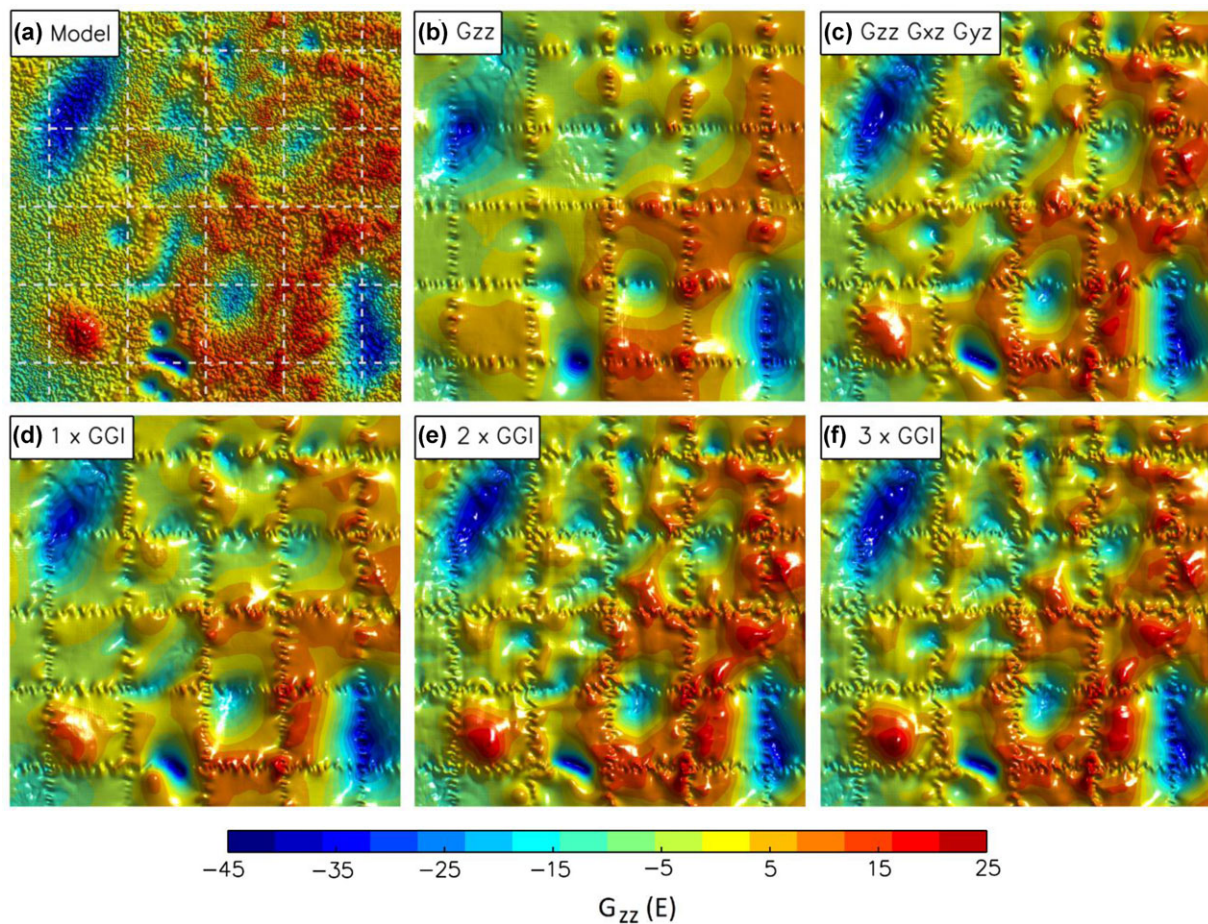


Figure 7 Reconstructed G_{zz} anomaly fields from inversions using different measurement groups. a) Exact answer, b) G_{zz} survey, c) G_{zz} , G_{xz} , G_{yz} survey, d) 1 GGI survey, e) 2 GGI survey, f) 3 GGI survey. Faint dashed lines on a) show the 4 km spaced N-S and E-W survey lines.

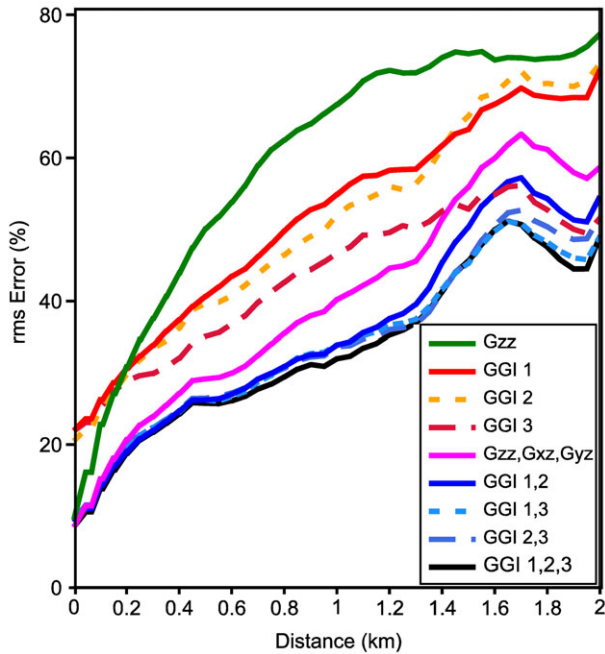


Figure 8 RMS error in the reconstructed anomaly fields as a function of distance from a measurement location. Error expressed as a percentage of the RMS signal at the same distance. The key indicates which measurement group was used in the processing.

where the regularization factor decreases with the distance to a measurement point, could have been implemented to better honour these data. However, for the purpose of promoting uniformity and isotropy in the processed data, a constant regularization scheme was employed for this analysis.

Recall that each GGI module of the FTG measures the two components of differential curvature in the plane of the spinning disk and because each module is tilted to the vertical, all measurements contain elements of the horizontal and vertical gravity gradients. There is a noticeable improvement when utilizing data from two modules (Fig. 7e and the blue lines of Fig. 8) compared to only using the data from a single module (Fig. 7d and the red lines of Fig. 8). Note, however, that a GGI orientated horizontally would produce more comparable results. The improvement when going from 2 to all 3 modules (Fig. 7f and the black line of Fig. 8) is less significant. Although the latter case provides all 6 components of differential curvature, there are only 5 linearly independent tensors and therefore the information content has not increased significantly from the 2 module case, having 4 components. This means that a 2-module system can reconstruct the field using an equivalent source inversion almost as well as the full 3-module FTG. A third GGI, does however, provide two ex-

tra independent measurements of the potential field, which contribute to the overall noise reduction of processed real FTG data. Outside of equivalent source inversions, measurements of the complete tensor also allow eigensystem analysis (FitzGerald, Holstein and Foss 2011) that can help determine the dimensionality of the source geometries.

Figure 9 shows the radial error PSDs of the different processed data sets divided by the radial PSD of the true anomaly signal (Fig. 3, solid line). It therefore shows the signal-to-error ratio (SER) spectral density as a function of radial wavenumber, $k = \frac{2\pi}{\lambda}$ (where λ is the radial Fourier wavelength, Blakely 1995). The error distributions were calculated as the differences between the processed anomaly fields and the exact forward-calculated model answer. As discussed above, these errors therefore include all effects of sampling and processing and provide the necessary insight into the useful resolution of the reconstructed field. Where the SER approaches 1, it signifies that the reconstructed field is not uniformly supported at these wavenumbers. Larger SER values show that the field is imaged accurately over these parts of the spectrum. Table 1 shows the useful resolutions of the data using two levels of confidence; where the error PSD is less than a) 70% and b) 50% of the anomaly signal (these correspond to lower limits on the spectral SER of 1.43 and 2, shown as horizontal dashed lines in Fig. 9). The 50% case builds in a high level of confidence where, if the data were low-pass filtered to these

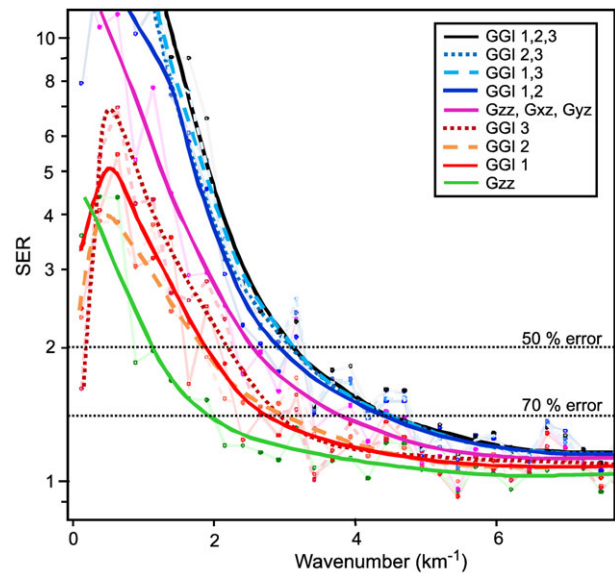


Figure 9 Radial PSD error analysis. Lines show the signal-to-error ratio (SER) spectra of the G_{zz} anomaly field for the different measurement cases considered. Faint lines and points show the actual PSD estimates and smoothed bold lines show the variation more clearly.

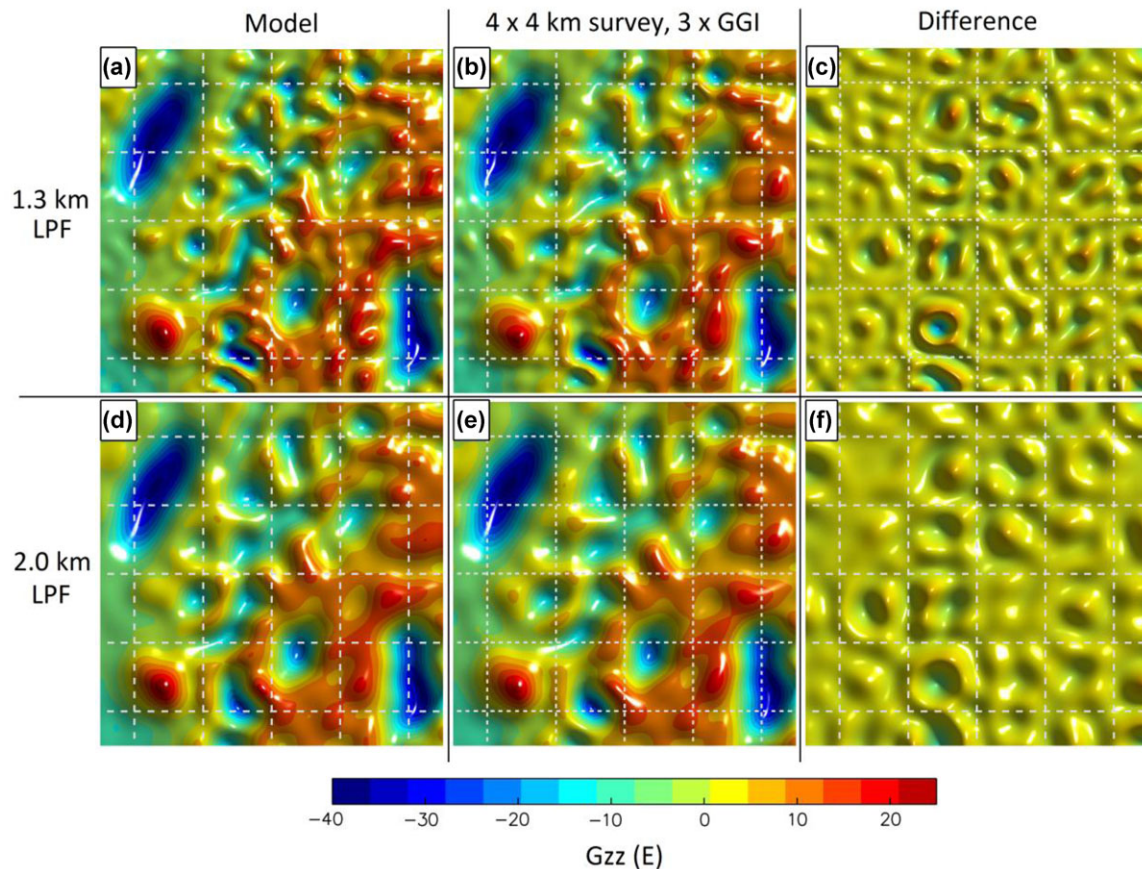


Figure 10 Reconstructed G_{zz} field from using measurements from all 3 GGIs of the FTG. a) and d) exact model answer, b) and e) reconstructed field from survey data, c) and f) difference (error) plots. Top row (a,b,c) is low-pass filtered to 1.3 km wavelength (<70% spectral error), bottom row (d,e,f) is filtered to 2.0 km (<50% spectral error). Dashed lines show flight line locations. The same colour scheme is used for all plots.

wavelengths, one could be confident that the resulting image accurately and consistently reproduces the true field. Filtering the data according to the 70% cases is near the limit of the useful resolution and, even though the radially averaged error PSD is less than 70% of the signal, it is spatially inconsistent with lower values near to the lines and unacceptably higher values in-between. Figure 10 shows these two situations for the full tensor (3 x GGI) case by comparing the reconstructed processed data to the model answer for low-pass filtering of 1.3 km (SER spectrum > 1.43, error < 70%) and 2.0 km (SER spectrum > 2, error < 50%). The latter case shows that the 4×4 km survey comfortably reproduces the true anomaly field with resolution down to 2 km wavelengths. Performing the error versus distance analysis for this case, Fig. 11 shows that the RMS spatial error is below 30% over the entire grid, further confirming that the data are accurate at this resolution even at the points furthest away from the survey lines.

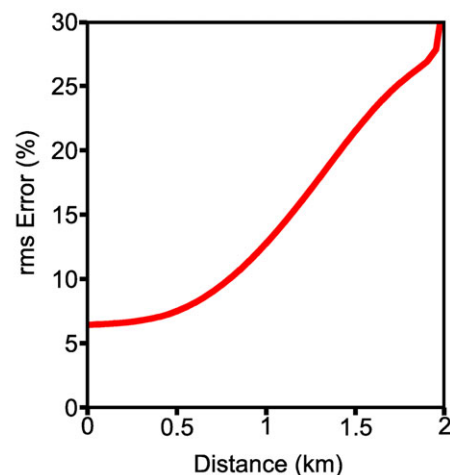


Figure 11 RMS error in the 2 km resolution anomaly field as a function of distance from a measurement point when using measurements of the full tensor on a 4×4 km survey.

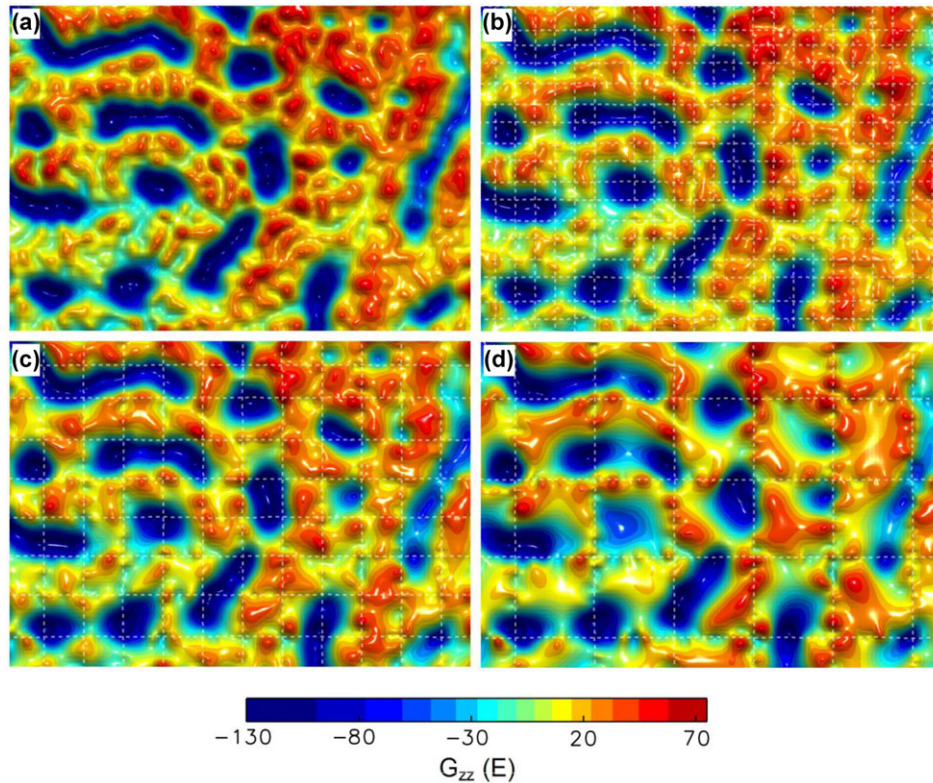


Figure 12 Reconstructed G_{zz} fields using FTG survey data with different line spacings. a) Truth, b) 1×1 km, c) 2×2 km, d) 4×4 km line spacing. Faint dashed lines show the survey line locations used in the processing.

FIELD EXAMPLE

To demonstrate how multi-component gravity gradient surveys with wide line spacing can reconstruct an accurate field in practice, we now look at an actual airborne FTG survey analysed at three different line spacings. The survey was flown for petroleum exploration over an area dominated by shallow salt bodies. Such features provide the large SNR and high-signal bandwidths required to undertake an accurate assessment of the effects of sampling. In order to resolve the finest details associated with the salt bodies and weathering layers, a survey with a tight line spacing of 120 m was acquired. More details of the geological setting and the survey parameters can be found in Barnes and Barraud (2012). With such tight line spacing, the processed data projected on a grid at a constant elevation can be considered to be an accurate representation of the total gravity gradient signal over its entire bandwidth.

Three sub-sampled surveys were constructed by selecting lines from the complete survey separated by the much wider spacings of (1×1) , (2×2) , (4×4) km. By processing only the data acquired along these selected lines, the error in the reconstructed field due to the sub-sampling can be estimated by comparing with the full survey case.

Figure 12 shows the reconstructed G_{zz} fields from the three sub-sampled surveys together with that deduced from the complete survey, all forward calculated to the same grid at an elevation of 50 m below the median flight height. The figures and analysis relate to an inner region of the entire survey representing roughly 20% of the total survey area. Processing of the FTG measurements followed the same procedure as outlined above, except that the signal from the terrain was retained to provide extra short-wavelength signal power to improve the error analysis (the terrain variation was actually quite low at <130 m and only provided a small contribution to the total signal power). The equivalent source models were designed accordingly without the topography to prevent knowledge of the terrain signals from being built into the inversion and therefore being predicted through the model geometry, rather than the survey measurements. Using real survey data, the equivalent source inversion also employed the simultaneous drift modelling described by Barnes and Lumley (2011) to remove time-domain drift in the line data.

Following the same PSD error analysis as before, Fig. 13 shows the error PSDs of the reconstructed G_{zz} fields from the 3 surveys together with the PSD of the truth signal. The ratios of

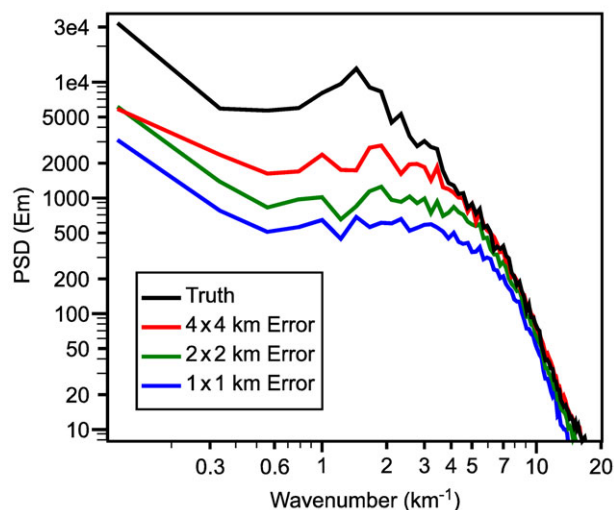


Figure 13 PSD G_{zz} error analysis. PSD of truth signal shown in black, coloured lines show PSDs of the error being the difference between the reconstructed and truth fields.

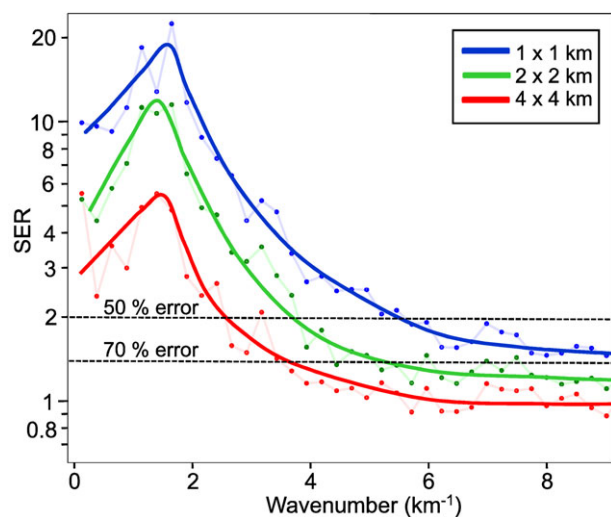


Figure 14 Signal-to-error ratio (SER) curves for the reconstructed G_{zz} for the 3 different sub-sampled surveys. The line spacing is indicated in the legend. Faint lines and points show the actual estimates and smooth solid lines show the variation more clearly.

these three curves with the truth signal give the signal-to-error ratios (Fig. 14). By reading off the bandwidths where the SER reduces to values of 2 and 1.43, the useful radial bandwidths at the 50% and 70% error limits can be estimated for each of the three line spacings, Table 2.

The 4×4 km sub-sampled survey is shown to provide useful bandwidths of 2.1 km (50% error limit) and 1.8 km (70% error limit), which compare well to the results from the synthetic model (2.0 km and 1.3 km, Table 1). It is likely to

Table 2 Useful resolutions of reconstructed G_{zz} data for the field example.

Error limit	1×1 km	2×2 km	4×4 km
70%	0.0 km	0.53 km	1.8 km
50%	1.1 km	1.7 km	2.5 km

be the noise in the field measurements that has reduced the extents of the useful bandwidths compared to the synthetic case. The reconstructed signal for the 4×4 km sub-sampled field case is therefore noise limited, rather than sampling limited. The 2×2 km and 1×1 km surveys, however, show little sign of noise limitation. With a tight enough line spacing and a suitable SNR in the individual measurements, the reconstructed field can predict the full bandwidth signal because the signal itself is band-limited due to the upward continuation of the potential field to the grid elevation. The 1×1 km survey has a spectral error $< 70\%$ over the entire bandwidth and can therefore be considered to reconstruct the full signal (at the grid elevation) adequately at all wavelengths. A comparison of Fig. 12(b) with Fig. 12(a) confirms visually that there is negligible loss of resolution in the sub-survey case. It is important to realize that the full signal is made up of several source contributions and that a particular geological target of interest might contribute only a small fraction of the total signal power. An adequate SER for the total signal does not necessarily mean suitable accuracy for the target signal. Errors that are small in the reconstruction of the total field could be large relative to the signal from the target. The imaging of these more subtle signals necessitated the tighter line spacing for the full-airborne survey to achieve the goals of the geological interpretation for this area.

CONCLUSIONS

When gravity gradient measurements are collected with a high SNR, the line spacing can be increased – therefore offering a way of reducing the duration and cost of an airborne or marine survey. The resolvability, rather than the detectability of the anomaly field, then becomes the limiting factor when choosing the line spacing. Such situations can arise when the anomalous signals of interest originate from shallow, localized sources with high-density contrasts producing large amplitude signals relative to the instrument noise. This often occurs in marine gravity gradient surveys where the slow speed allows significant reductions in noise bandwidth. The field example showed an airborne survey that approached this situation

where a large SNR was provided by shallow salt bodies. In the future, this situation will occur more often as the raw measurement noise decreases due to improvements in technology.

To estimate the resolution achievable from a survey with wide line spacing, known gravity gradient fields were calculated and sub-sampled by a simulated airborne survey pattern. No noise was added to the data so that the errors and limits of resolution originated from only the sparse sampling and the equivalent source processing scheme used to combine, transform and grid the data. It was shown that with this scheme, a gravity gradient system with 2 GGIs, measuring 4 components of differential curvature according to the FTG umbrella configuration, can reconstruct the field almost as well as the complete tensor system having 3 GGIs. Table 1 summarizes the useful resolutions of grids of G_{zz} data resulting from processing data flown along N-S and E-W lines separated by 4 km with different groups of components measured. This analysis quantified the increase in resolution that can be expected when acquiring multiple components of the gravity gradient field. With simulated measurements from a full-tensor system, a gridded G_{zz} data set was produced and shown to have RMS errors between 6–30% when filtered to a full-wavelength of 2 km. The smaller errors occurred near to the measurement points and the highest errors occurred midway between the survey lines. The 2 km filter was determined by analysing the radial PSD of the error and specifying the useful resolution as the bandwidth over which the signal PSD is at least twice the error PSD. This signal-to-error ratio of 2 corresponds to a stringent level of confidence but ensures that the quoted resolution of 2 km represents a bandwidth over which the reconstructed anomaly field is uniformly and consistently accurate. The field example reached similar conclusions showing that such resolutions can be achieved in practice, provided that the target anomaly provides a sufficient signal-to-noise ratio. Without this condition, surveys are forced to tighter line spacing to reduce noise and then the advantage of measuring multiple tensor components reduces since the Nyquist limits of the sampling pattern will already exceed the bandwidth of the target signal. Such a situation starts when the line spacing is commensurate with the size or the depth to the target.

ACKNOWLEDGEMENTS

We are grateful to Maurel et Prom for granting permission to present the field data. Des FitzGerald provided valuable comments and discussions on the topic of this paper. Thanks are also due to editors M. Fedi, I. Elysseieva and two reviewers for

their comments and suggestions that resulted in an improved version of the manuscript.

REFERENCES

- Barnes G. 2012. Interpolating the gravity field using full tensor gradient measurements. *First Break* 30, 97–101.
- Barnes G. and Barraud J. 2012. Imaging geologic surfaces by inverting gravity gradient data with depth horizons. *Geophysics* 77(1), G1–G11.
- Barnes G.J., Barraud J., Lumley J. and Davies M. 2008. Advantages of multi-tensor high resolution gravity gradient data. 78th Annual International Meeting, SEG, Expanded Abstracts, 3587–3590.
- Barnes G. and Lumley J. 2011. Processing gravity gradient data. *Geophysics* 76(2), I33–I47.
- Barnes G.J., Lumley J.M., Houghton P.I. and Gleave R.J. 2011. Comparing gravity and gravity gradient surveys. *Geophysical Prospecting* 59(1), 176–187.
- Blakely R.J. 1995. *Potential Theory in Gravity and Magnetic Applications*. Cambridge University Press.
- Brewster J. 2011. Description and evaluation of a full tensor interpolation method. *SEG Expanded Abstracts* 30, 811–814.
- Brewster J. 2012. Full tensor interpolation: Evaluation of the effect of line spacing and noise. *SEG Expanded Abstracts* 31, 1–5.
- Brzezowski S.J. and Heller G.H. 1988. Gravity gradiometer survey errors. *Geophysics* 53(10), 1355–1361.
- Dampney C.N.G. 1969. The equivalent source technique. *Geophysics* 34, 38–53.
- FitzGerald D.J. and Holstein H. 2006. Innovative data processing methods for gradient airborne geophysical data sets. *The Leading Edge* 25, 87–94.
- FitzGerald D., Holstein H. and Foss C. 2011. Automatic modelling and inversion for dykes from magnetic tensor gradient profiles – Recent progress. *SEG Expanded Abstracts* 30, 796–800.
- FitzGerald D.J., Paterson R. and Holstein H. 2012. Comparing two methods for gridding and honouring gravity gradient tensor data. 74th Annual International Conference & Exhibition, EAGE, Extended Abstracts.
- Jekeli C. 1993. A review of gravity gradiometer survey system data analyses. *Geophysics* 58(4), 508–514.
- Mendonça C.A. and Silva J.B.A. 1995. Interpolation of potential-field data by equivalent layer and minimum curvature: A comparative analysis. *Geophysics* 60(2), 399–407.
- Pedersen L.B. and Rasmussen T.M. 1990. The gradient tensor of potential field anomalies: Some implications on data collection and data processing of maps. *Geophysics* 55(12), 1558–1566.
- Pilkington M. 2012. Analysis of gravity gradiometer inverse problems using optimal design measures. *Geophysics* 77(2), G25–G31.
- Reid A.B. 1980. Aeromagnetic survey design. *Geophysics* 45, 973–976.
- Rim H. and Li Y. 2012. Single-hole imaging using borehole gravity gradiometry. *Geophysics* 77(5), G67–G76.
- While J., Biegert E. and Jackson A. 2008. Interpolation of gravity and gravity gradient data by using the generalized sampling expansion: Theory. *Geophysics* 73(2), 111–121.